JOURNAL OF SPACECRAFT AND ROCKETS
Vol. 45, No. 6, November–December 2008

Ground Test Studies of the HIFiRE-1 Transition Experiment Part 2: Computational Analysis

Matthew MacLean,* Timothy Wadhams,* and Michael Holden†
Calspan–University at Buffalo Research Center, Buffalo, New York 14225
and
Heath Johnson‡
University of Minnesota, Minneapolis, Minnesota 55455

DOI: 10.2514/1.37693

Comparisons to measurements made in the Calspan–University at Buffalo Research Center LENS I facility on a full-scale HIFiRE-1 vehicle at duplicated flight conditions have been made with the computational fluid dynamics code DPLR and the parabolized stability equation code STABL. These comparisons include laminar heating, transition onset, turbulent heating, and turbulent flare separation for the test article at 0 deg angle of attack. Predictions of transition onset with the parabolized stability equation algorithm correlate to an average *N* factor of 5.7 with a standard deviation of 0.75 and show the proper trend with regard to entropy-layer and boundary-layer effects. Extrapolating the parabolized stability equation solutions to the most likely flight environment will lead to a delay in onset of approximately 20 cm on the forebody. On the turbulent forebody, heating predictions compared with ground test measurements have shown that Reynolds average Navier–Stokes turbulence models can overpredict the measurements by up to 30%, and initial investigations suggest that this discrepancy may be linked to total-to-wall-temperature ratio. In the interaction region, the most popular Reynolds average Navier–Stokes models in their nominal form fail to capture the necessary features of the flowfield; however, proper limiting of the Reynolds stress tensor can accurately predict the size of the separated region and provide sufficiently good agreement for a design level calculation.

Nomenclature

C_{b1}	=	production coefficient in Spalart–Allmaras model
C_F	=	skin friction coefficient
C_H	=	Stanton number
C_{LIM}	=	Reynolds stress limiter coefficient in shear stress transport model
d	=	distance from the wall in Spalart–Allmaras model
F_2	=	blending function in shear stress transport model
k	=	turbulent kinetic energy
n	=	Reynolds analogy exponent
Pr	=	Prandtl number
S	=	vorticity in Spalart–Allmaras model
$\alpha_1, \alpha_2, \Gamma$	=	coefficients in SALSA modification
κ	=	Kármán constant
μ_T	=	eddy viscosity
ν	=	molecular kinematic viscosity
$\tilde{\nu}$	=	Spalart–Allmaras variable
ρ	=	density
Ω	=	vorticity in shear stress transport model
ω	=	turbulent dissipation

Presented as Paper 0641 at the 46th AIAA Aerospace Sciences Meeting and Exhibit, Reno, NV, 7–10 January 2008; received 24 March 2008; revision received 16 June 2008; accepted for publication 1 July 2008.

*Senior Research Scientist, Aerothermal/Aero-optics Evaluation Center. Member AIAA.
†Vice President of Hypersonics, Aerothermal/Aero-optics Evaluation Center. Fellow AIAA.
‡Senior Research Associate, Department of Aerospace Engineering and Mechanics. Senior Member AIAA.

I. Introduction

FULLY duplicated ground test experiments have been performed in the CUBRC (Calspan–University at Buffalo Research Center) LENS I shock-tunnel facility to develop and validate the design of the first in a series of flight test experiments intended to study fundamental phenomena relevant to hypersonic and hypervelocity flows. This test program studied a full-scale flight vehicle at selected conditions along the test flight trajectory and has included both the experimental component and a parallel computational effort to validate the experiment and numerical modeling. The experimental results of the test program are fully discussed separately [1]. This paper focuses on Navier–Stokes computations performed in support of the ground test experiments to model these physical phenomena and maximize the potential of the design to return good-quality, relevant flight data when the flight occurs. Calculations are shown covering the topics of laminar forebody heating, prediction of transition in the shock-tunnel facility and in flight, turbulent forebody heating, and turbulent shock interaction in the separated region on the flare.

The goal of the Hypersonic International Flight Research and Experimentation (HIFiRE) program is to develop hypersonic technologies by focusing on specific deficiencies in the capabilities to design next-generation hypersonic vehicles. For each HIFiRE configuration, results from a low-cost flight test will be compared with ground test data and numerical predictions to assess deficiencies in design tools and improve computational and physical models. The first vehicle, HIFiRE-1 (formerly called FRESH-FX), features three segments, which include a blunted-cone forebody, a cylindrical midbody, and a flared aftbody designed to generate a turbulent separated region. The focus of this flight includes experiments on boundary-layer transition and on turbulent separated flows [2]. In support of the first flight test, extensive studies have been performed by CUBRC in the LENS I facility to design several aspects of the experiment, principally the nosetip radius, the flare angle and size, and boundary-layer tripping on the conical forebody. Selection of the nosetip radius is critical to the goal of obtaining natural transition on the conical forebody over much of the trajectory of the flight, which

will be dominated by the influence of the entropy layer on the stability of the boundary layer. Selection of the flare angle and size is necessary to ensure a well-posed experiment for computational code validation by picking an angle, which allows a meaningfully large separated region while allowing sufficient length for reattachment on the downstream flare.

II. Experimental Facility Background

Currently, CUBRC operates the 48 in. reflected shock tunnel, the LENS I and LENS II reflected shock tunnels [3], and the LENS XX expansion tunnel [4] shown in Fig. 1. The reflected shock tunnel uses incident and reflected shocks to cleanly heat and pressurize a stagnant test gas to high enthalpy levels. This test gas may then be expanded through a converging–diverging nozzle in a manner similar to a blowdown facility to produce a hypervelocity test flow. Expansion tunnels like LENS XX also operate as short duration facilities, but an expansion tunnel produces a high enthalpy flow by adding kinetic energy directly to the flow by expanding through an accelerant gas. Because the flow is never stagnated, the expansion tunnel produces a quiescent freestream state that minimizes the thermal and chemical nonequilibrium that occurs in the freestream of reflected shock tunnels at very high enthalpies (greater than 5 MJ/kg). CUBRC employs both reflected shock and expansion tunnels to provide a wide range of supersonic, hypersonic, and hypervelocity test capabilities, which are summarized in Fig. 2. The nominal trajectory planned for the HIFiRE-1 flight is noted along with specific test points duplicated in the facility during the ground test.

The LENS reflected shock-tunnel facilities were developed primarily to study the full-scale, hypervelocity flow physics of interceptors and airbreathing engine configurations. The scale and flow duplication capabilities of LENS are such that these vehicles can be studied at their full scale, inclusive of effects such as transition to turbulence, turbulent mixing from crossflow jets and thrusters, duplicated flow chemistry, and other effects that are difficult or impossible to simulate at cold-flow or subscale conditions. The reflected shock-tunnel facilities have been validated with tests of measurements by comparing directly to numerical predictions, including recent work with tunable laser-diode diagnostics [5,6]. Additionally, the facilities have been used to perform studies of fundamental flow phenomena, like the double cone, with success and to solve practical flight problems on vehicles like the shuttle space transportation system vehicle.

III. Numerical Tools

A. Data-Parallel Line Relaxation Code

All ground test studies in the LENS facilities are extensively calibrated and validated with numerical tools. The primary CFD (computational fluid dynamics) tool used is the DPLR code provided by NASA Ames Research Center. DPLR is a multiblock, structured, finite-volume code that solves the reacting Navier–Stokes equations including finite rate chemistry and finite rate vibrational nonequilibrium effects. This code is based on the data-parallel line relaxation method [7] and implements a modified (low dissipation) Steger–Warming flux splitting approach [8] for the convection terms and central differencing for the diffusion terms. Finite rate vibrational relaxation is modeled via a simple harmonic oscillator vibrational degree of freedom [9] using the Landau–Teller model [10]. Vibrational energy relaxation rates are computed by default from the semi-empirical expression due to Millikan and White [11], but rates from the work of Camac [12] and Park et al. [13] are substituted for specific collisions where experimental data exists. Vibration-dissociation coupling is currently modeled using the T-Tv approach of Park [14] or with some preliminary implementation of coupled-vibration-dissociation-vibration coupling [15]. Transport properties are appropriately modeled in DPLR for high enthalpy flow [16,17] using the binary collision-integral-based mixing rules from Gupta et al. [18]. Diffusion coefficients are modeled using the self-consistent effective binary diffusion (SCEBD) method [19]. Turbulence models available in the DPLR code currently include the Baldwin–Lomax 0-equation model [20], the Spalart–Allmaras 1-equation model [21], and the shear stress transport (SST) 2-equation model [22] each with corrections for compressibility effects [23,24].

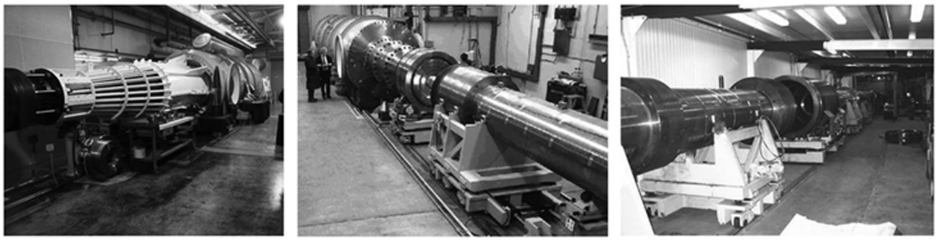

a) Lens I b) Lens II c) Lens XX

Fig. 1 LENS facilities at CUBRC.

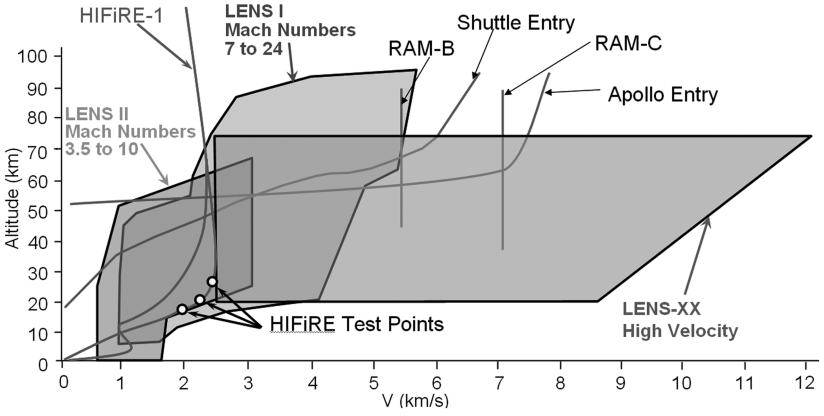

Fig. 2 Velocity-altitude duplication capabilities of CUBRC LENS Facilities.

Table 1 Summary of nominal flight condition points duplicated in LENS tests [1]

Condition	Velocity, m/s	Altitude, km	Temperature, °K	Pressure, kPa	Density, kg/m^3	Mach number	Re/m $\times 10^6$
A	1927	17.8	214.4	7.73	0.124	6.58	17.4
B	2183	21.1	231.7	4.62	0.072	7.16	10.2

Recent relevant capabilities of the DPLR code involve automated grid adaptation to improve solution quality [25].

B. STABL Code

The STABL (stability and transition analysis for hypersonic boundary layers) package [26–28] is a comprehensive suite of tools that features an integrated two-dimensional/axisymmetric chemically reacting laminar flow solver, equilibrium chemistry tool, parabolized stability equation (PSE) solver, post-processor and various supporting tools, and scripting wizards integrated into a single, intuitive, Perl-based GUI interface. The CFD and PSE solvers use message passing interface for efficient parallel processing.

The PSE solver is a primary part of the STABL suite that solves the parabolized stability equations for two-dimensional or axisymmetric flow derived from the Navier–Stokes equations. The PSE equations are developed by modeling instantaneous flow variables with a mean and fluctuating component and subtracting the mean component from the resulting equation set. The result is a system of second-order partial differential equations for the disturbances, which are parabolized according to Herbert's [29] method by assuming that the disturbances are composed of a fast-oscillatory wave part and a slowly-varying shape function. The ellipticity of the wave part is preserved while only the governing equation for the shape function is parabolized. Assuming that initial disturbances are small and making an assumption of locally parallel flow at the starting plane allows sufficient simplification to generate an initial solution for the shape function and complex streamwise wave number. These initial solutions may then be marched downstream using the parabolized stability equations.

The PSE analysis generates a prediction for the evolution of an initial disturbance as it moves downstream from its starting point through the mean flowfield. To predict the onset of transition, an experimental correlation is required. STABL uses the semi-empirical e^N correlation method. Experimental studies have shown N to be about 8–11 for quiescent flight environments [30–32] and levels around 5.5 (sometimes lower) for tunnel environments [33,34] where freestream noise levels can be somewhat larger.

IV. Review of Ground Test Data and Experimental Setup

The ground test experiments have been completed in two phases. These experiments are discussed in better detail in another publication [1], and so only a brief review will be given in this section. In the first phase, the objective was to perform a basic investigation of the flow phenomena and to design several features of the flight vehicle. The CUBRC ground test model is a full-scale representation of the anticipated flight vehicle, and the ground tests were performed at duplicated flight conditions to those anticipated for a nominal descent trajectory at key points along the flight path. The primary conditions are listed in Table 1 for two points that were shown on the trajectory in Fig. 2. The vehicle, as installed in the LENS I facility, is shown in Fig. 3.

In the first phase, four axial rays of thin-film heat transfer gages were arranged along the conical forebody and cylindrical midbody to assess the approximate transition-onset point and turbulent heating profile on the vehicle. The nosetip was made to be removable, and several different nose radii, from sharp to 5.0 mm, were tested. Because the flare angle was undetermined at the outset of the phase I program, the turbulent separated region was monitored via Schlieren imagery, and several different flare angles from 27 to 37 deg were employed to size the flare qualitatively. Runs were made at Mach numbers of 6.6, 7.2, and 7.4 at 0, 1, and 5 deg angle of attack. The basic vehicle dimensions and summarized instrumentation totals used in phase I are shown in Fig. 4.

At the conclusion of the phase I study, a nose radius of 2.5-mm and a flare angle of 33 deg were selected as the recommended flight configuration based on the phase I experiments and corresponding CFD analysis described here. For the second phase, the ground test model was configured with these geometries, and a significant amount of instrumentation was added to better define the aerothermal characteristics of the vehicle. A number of heat transfer gages were added to the primary ray in the transition region to better measure natural transition onset and the intermittency process. This same instrumentation was also used to study the effects of the single trip to be placed at one angular location on the flight vehicle by testing the trip effectiveness over a range of Reynolds numbers. Finally, a heavily instrumented insert was placed at the cylinder/flare junction on the primary ray to make quantitative measurements in the separated region over the flare. This additional instrumentation including the flare insert is also summarized in Fig. 4.

The combined, two-phase program has generated a data set of approximately 50 runs on a full-scale HIFiRE-1 model at conditions completely duplicating the nominal trajectory and flight dispersions. The integrated effort of the experimental results and the supporting computational analysis presented here is packaged as a database with three primary purposes: 1) as a stand-alone code validation data set, 2) as a database for design of the flight vehicle, and 3) for comparison with the future flight data when it becomes available.

The major features of interest on this geometry are shown in Fig. 5, which shows contours of a typical flowfield. The major features of the flow that are considered in this numerical study are the natural

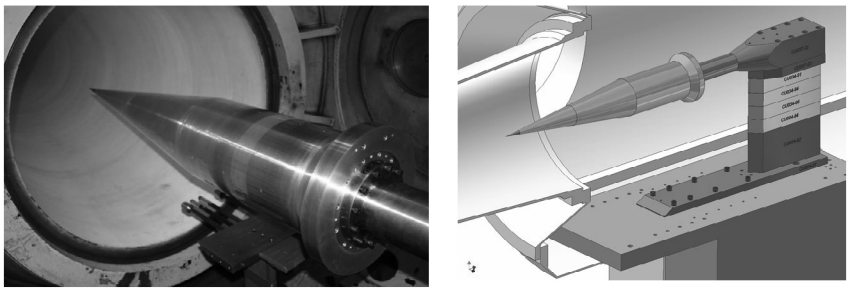

a) Installed photo **b) CAD rendering**

Fig. 3 HIFiRE-1 ground test model shown in LENS I facility.

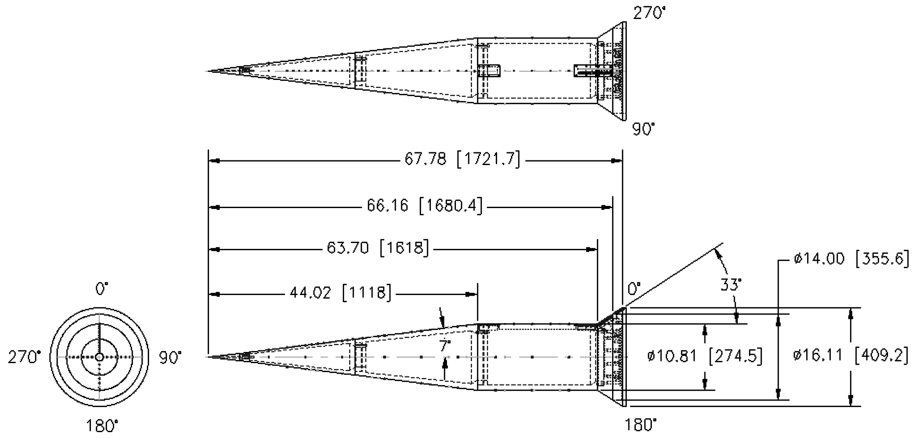

NUMBER OF INSTRUMENTS PER SECTION								
	CONE		CYLINDER		FLARE		EXTENSION	
	HEAT	PRES	HEAT	PRES	HEAT	PRES	HEAT	PRES
PHASE I	32	6	17	4	0	0	0	0
PHASE II	47	11	33	28	17	17	9	4

Fig. 4 HIFiRE-1 ground test model and instrumentation layouts (dimensions in inches [mm]).

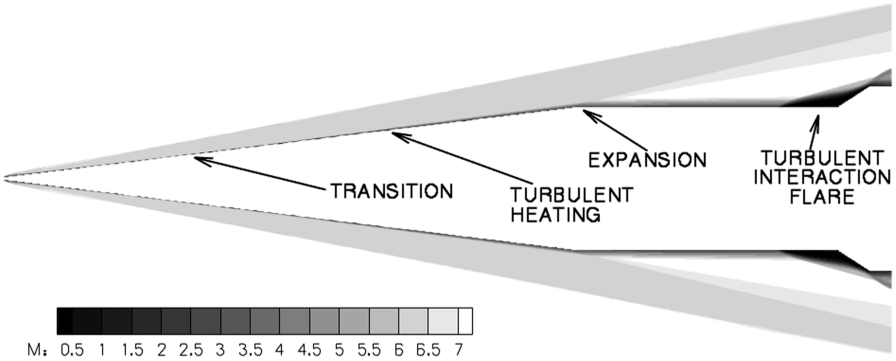

Fig. 5 Overview of complete HIFiRE-1 flowfield calculation showing Mach number contours and major flow features of interest.

(untripped) transition process on the conical forebody, turbulent heating on the cone, the expansion of the turbulent flow onto the cylindrical midbody providing entry flow to the flare, and the turbulent boundary-layer/shock interaction on the flare surface.

V. Comparison of Calculated Laminar Forebody Heating and Estimation of Transition Onset

The most basic component of the validation process has been our rigorous effort to validate the freestream test conditions generated in the facility during the two phases. In addition to pretest airflow calibrations where arrays of probes are placed in the test section and comparisons are made to full Navier–Stokes simulations of the nozzle expansion flowfield [35,36], we performed simulations of the forebody of the vehicle for each test condition and compared them with the laminar heating data measured on the cone. These comparisons have been made for most of the runs at 0 deg angle of attack where an axisymmetric solution can be made with DPLR in a time frame that keeps pace with the rate at which the facility runs are made.

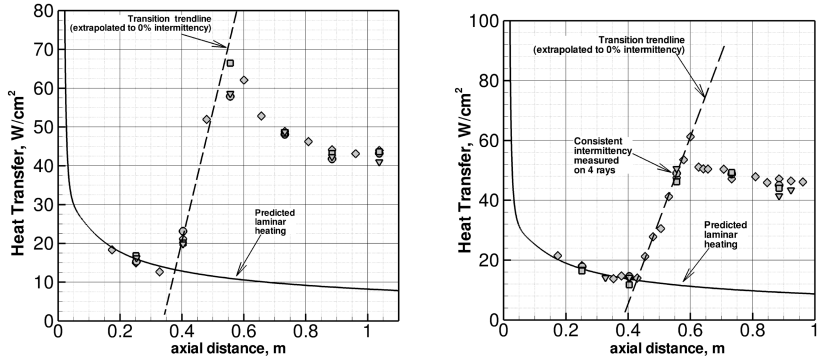

a) Condition A sample (M=6.58, run 4) **b) Condition B sample (M=7.16, run 30)**

Fig. 6 Typical comparisons of experimental data on HIFiRE-1 ground test model with DPLR prediction of laminar forebody flow for 2.5-mm nosetip.

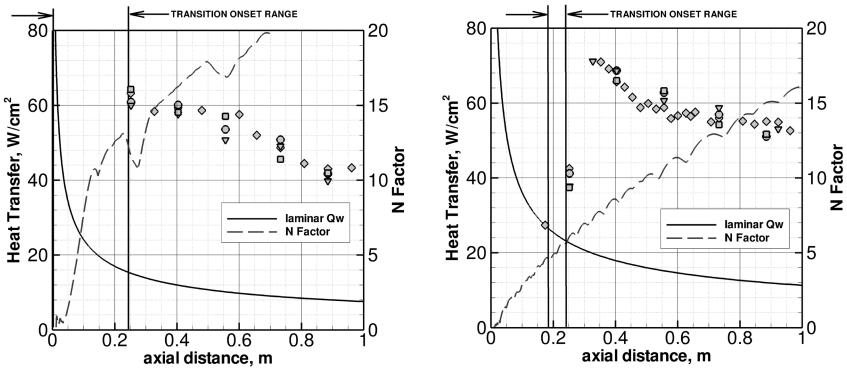

a) Condition A (M=6.58, run 3) b) Condition B (M=7.16, run 36)

Fig. 7 Comparison of experimental heating on axisymmetric HIFiRE-1 ground test model with DPLR laminar heating prediction and STABL second-mode growth for sharp-nosetip configuration.

Examples of this comparison are shown in Fig. 6 for two cases representing the two nominal test conditions that were outlined in Table 1. Several runs were made at each of these two test conditions and several off trajectory permutations were tested as well, but the agreement shown in Fig. 6 is typical of all runs and represents the quality of the complete data set. For all points which remain laminar, the agreement is well within the uncertainty of the measurement and the CFD simulation. The excellent correlation between the four rays of data should also be noted, particularly in the intermittency region. Finally, the cases shown were taken from the phase I data set for Fig. 6a and from the phase II data set for Fig. 6b to illustrate the improvement in defining the transition region by the addition of the extra primary ray sensors.

More important, doing this comparison allows the transition-onset point to be estimated by selecting the point at which the data begins to depart from the laminar solution. Methods for determining the transition-onset point have been described previously [37] and include the commonly applied method of extrapolating a trend line back to zero intermittency, qualitative analysis of the intermittent fluctuations in the heating level measured by the thin-film heat flux sensors, and quantitative statistical analysis of those intermittent fluctuations. These methods will predict a range of transition-onset locations that can result in significant uncertainty in the position at higher Mach numbers, but, at these conditions, transition occurs rather abruptly, and we can pick the location accurately with the simple trend line method. Regardless of the technique chosen, the best resolution that one can obtain is limited by the spacing of the sensors in the transition region. For example, in the case of run 4, shown in Fig. 6a, transition can be bounded between 0.35 and 0.4-m, with an average of 0.375-m. This is consistent with the point at which the transition trend line crosses the laminar heating profile.

The measured transition-onset locations on the model were compared with simulations performed with the STABL code to predict second-mode transition for all cases in which the model was at 0 deg angle of attack. Additional transition data was measured for conditions at angle of attack as part of the experimental program [1], but the inherent additional complexities of crossflow instabilities are not considered here. Three different nose radii were tested (sharp, 2.5-mm, and 5.0-mm). Several of these cases primarily from the phase I study have been published previously [38,39], and so only some cases that have implications on this discussion are shown. For each case, a window of uncertainty has been placed between the last definitively laminar gage position and the point at which the measurement is observed to have notable intermittency. Our analysis indicates that transition onset has occurred within this window of uncertainty. In all cases, the trend line extrapolating to zero intermittency (the onset point) falls at about the middle of the window.

The sharp-nose cases are considered first with results shown in Fig. 7. A sharp nosetip is infeasible for a flight vehicle but provides a useful limiting case. As shown in Fig. 7a, the gages for the phase I model were placed such that the first measurement is already fully turbulent for run 3. The transition-onset point cannot be determined for this case, and so it is only possible to say that onset occurred at some station less than $X = 0.25$ m. However, comparison with the prediction of the STABL code indicates that the N factor has already increased to more than 13.0 at $X = 0.25$ m, and so the expected result is at least consistent with the measurements. In Fig. 7b, however, the additional instrumentation incorporated in the phase-II model increased the measurement density sufficiently to pick up the laminar region of the flow and bound the onset location as shown for run 36. Assuming the same median N factor of 5.3 to hold for run 3, the transition location would have been at 8.3 cm from the sharp tip.

Several cases were considered for the 2.5 mm nosetip, which was the eventual nosetip configuration chosen for flight. One case is shown in Fig. 8 for condition A and two cases for condition B are shown in Fig. 9. For the condition B test point, a run was made in phase I given in Fig. 9a and then this same run was repeated in phase II with the extra instrumentation as shown in Fig. 9b. Comparing these two runs shows the improvement in picking the transition-onset location by adding the phase II instrumentation. For run 5 (phase I), STABL computes an N factor of 6.8 at transition onset with an uncertainty of ± 1.0 (range of 5.8–7.8) based on the window of possible onset location. For run 30, STABL computes an N factor of 6.5 at nominal transition onset with an uncertainty of ± 0.25 (range of 6.25–6.75). These two runs are statistically consistent in their prediction of transition onset. However, the additional gages improve the onset estimation uncertainty by a factor of 4 times. For both condition A and condition B, natural transition onset occurs near $X = 0.4$ m, which is midway down the body and provides a region of both laminar flow and turbulent flow before the corner expansion that occurs near $X = 1.1$ m.

The preliminary flight test article design was for a 5.0 mm nosetip, and so this geometry was replicated in the ground test model also.

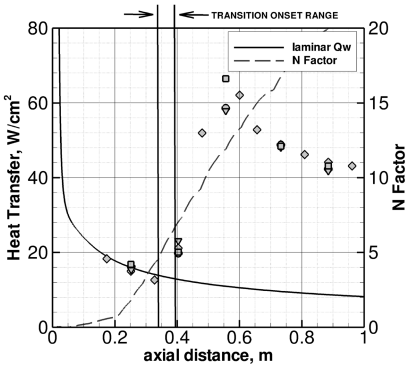

Fig. 8 Comparison of experimental heating on axisymmetric HIFiRE-1 model with DPLR laminar heating prediction and STABL second-mode growth for 2.5-mm nosetip configuration for condition A (Mach 6.58, run 4).

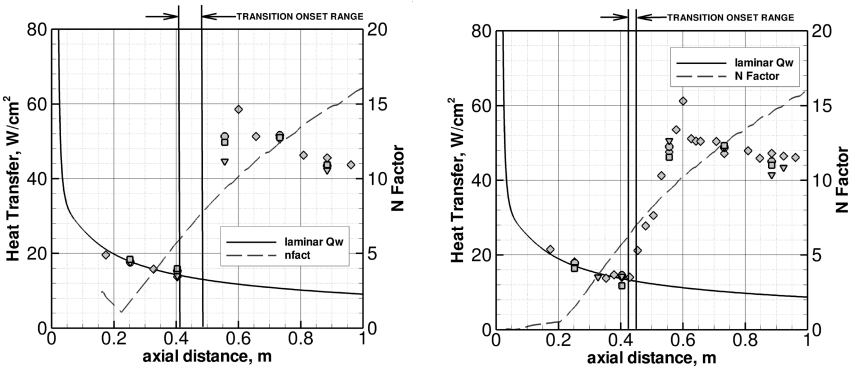

a) Phase I case (run 5) b) Phase II case (run 30)

Fig. 9 Comparison of experimental heating on axisymmetric HIFiRE-1 model with DPLR laminar heating prediction and STABL second-mode growth for 2.5-mm nosetip configuration for repeated runs at condition B (Mach 7.16).

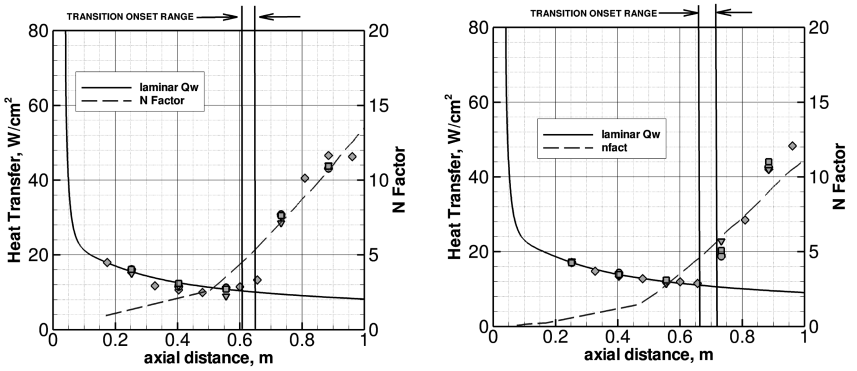

a) Condition A (M=6.58, run 8) b) Condition B (M=7.16, run 7)

Fig. 10 Comparison of experimental heating on axisymmetric HIFiRE-1 ground test model with DPLR laminar heating prediction and STABL second-mode growth for 5.0-mm nosetip configuration.

Cases with the 5.0 mm nosetip radius at the primary test conditions are shown in Fig. 10. With this nose radius, transition is pushed back to the aft end of the cone with no clearly defined equilibrium turbulent region upstream of the expansion. These measurements and accompanying STABL solutions were the primary reason for our selection of the 2.5 mm nose radius as a better choice for the flight vehicle to obtain laminar and turbulent natural heating over a sufficiently large range of the trajectory. As indicated by both the experimental and computational data, the 5.0-mm radius delays transition too much to get a good turbulent heating level without trips.

The comparison with the STABL solutions for this complete set of cases show that the PSE solver is responding to the change in nosetip radius because instability growth is suppressed more within the larger entropy layer. From the results presented, one can see that the region of suppression increases with a larger nose radius, resulting in smaller second-mode N-factor growth at a given station. By using the measured transition stations, we observe that the range is bounded within a relatively narrow region of N-factor growth. Discounting run 3, for which no definitive onset point can be determined, the range of the seven runs is 4.9 to 6.8, with an average N factor of 5.7. This value is similar to the accepted value of 5.5 for ground test facilities. The standard deviation of this set is 0.75. We note that in previously published work [37], including experiments at higher Mach numbers, a larger range of possible N factors was found with values on a similar cone up to 7.0 and somewhat larger values observed on a compression surface. Although this limited data set begins to build a database of transition data in the LENS facilities, we emphasize that it is not obvious that the amplitude growth should be exactly constant across the wide range of Reynolds number and Mach number conditions in which we operate the facilities. Still, based on the information collected thus far, the effects of transition seem to be repeatable and predictable when the experiment is combined with the STABL solution.

Finally, the results obtained in the ground test study are extrapolated to flight by using the DPLR and STABL tools after we have gained confidence in their predictive capability for this flowfield. The ground test is a full-scale, fully duplicated clone of the nominal flight and therefore replicates the future flight in every way except two, potentially. The first potential difference is the noise environment, which has just been shown to cause transition with an average growth N factor of 5.7. The growth rates required to produce natural transition in flight are far less understood, but we will take the accepted value range of 8–11 for the purpose of design. The second potential difference is the wall temperature, which is fixed at 300 K for the ground test. Again, the flight condition is more nebulous, but the preflight estimates by Kimmel et al. [2] showed that the surface temperatures for this part of the trajectory will be at least close to radiative equilibrium. In any case, the radiative equilibrium surface boundary condition was chosen to perform a worst-case analysis and serves as a bounding limit. The nominal conditions A and B were used to compute the mean flow with DPLR using the radiative equilibrium surface boundary condition and the instability growth computed in STABL. The predicted surface temperature profiles for the two conditions are shown in Fig. 11. In Fig. 12 the N-factor growth predictions are shown for the two cases with the possible range of transition in this part of the trajectory highlighted. This result confirms the conclusion from the experimental data that the 2.5-mm nosetip is a good choice. The uncertainty in the flight transition point onset is large, but assuming transition onset occurred in the middle of the possible range for flight would yield transition at 0.58 m for condition A and 0.65 m for condition B. When comparing with the compatible ground test runs (Figs. 8 and 9), the transition point moves aft by approximately 20 cm (8 in.) in each case. The change in

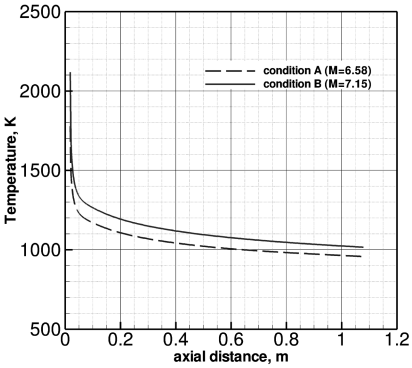

Fig. 11 Predicted surface temperature profiles for nominal flight trajectory points using radiative equilibrium.

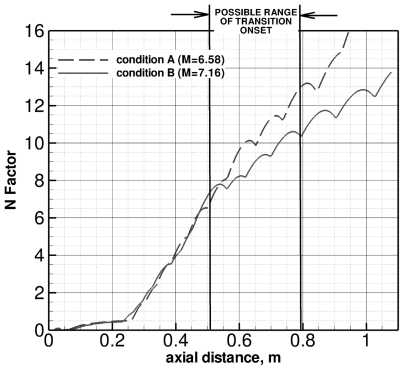

Fig. 12 Predicted second-mode instability growth for the radiative equilibrium flight vehicle.

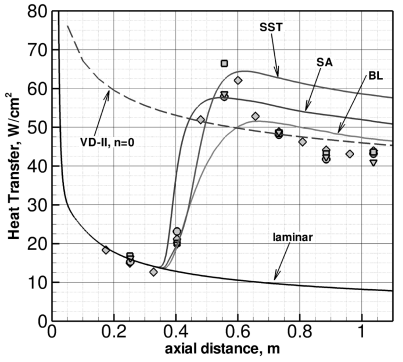

Fig. 13 Comparison of predicted and measured turbulent cone heating for 2.5-mm nose at condition A (Mach 6.58, run 4).

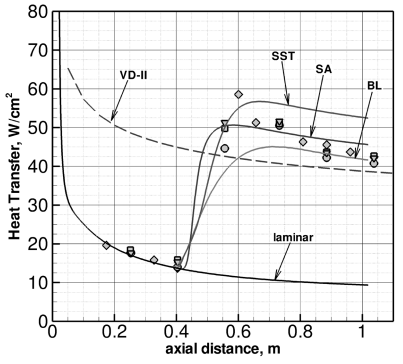

Fig. 14 Comparison of predicted and measured turbulent cone heating for 2.5-mm nose at condition B (Mach 7.16, run 5).

the onset position can also have an effect on the length of transitional region before equilibrium turbulence is observed and should be considered in the design of the flight vehicle. Finally, the hot-wall boundary produced almost no change in the instability growth on the vehicle for these conditions. This was verified experimentally in the ground test by heating the nose up to about 550 K (1000 deg R), which produced the same transition profile as without the additional heating [1]. This combined experimental and computational analysis suggests that smooth body transition should be observed on the forebody of the vehicle with some posttransition turbulent running length in flight.

VI. Comparison of Calculated Turbulent Forebody Heating to Experiment

Prediction of the turbulent forebody heating is more difficult. Here, a series of RANS (Reynolds-averaged Navier–Stokes) models has been employed to predict turbulent heating given the known transition-onset point. The effect of laminar-turbulent transition onset in DPLR has been modeled simply by suppressing all production terms up to the X station specified to the code [40], where this point has been determined from the experimental data and stability analysis. For the algebraic Baldwin–Lomax model, this amounts to setting the turbulent viscosity to zero up to that point and then computing it directly based on the algebraic dependence to the boundary-layer profile as normal. For the transport-level turbulence models, the production source terms were set to zero up to that point, implying a more complex relationship between the specified onset point (when the production source term is included in the transport equation) and the observed rise in heat transfer in the solution data.

The predicted turbulent heating results are compared with the experimental results in the equilibrium turbulent region for the two primary test conditions in Figs. 13 and 14 using the 2.5 mm radius nosetip. In both cases, the results are similar. The simplest model, Baldwin–Lomax (abbreviated BL in the figure) performs best at these conditions for the zero pressure gradient flow. The Spalart–Allmaras model (abbreviated SA in the figure) performs second best, predicting a heating level just higher than the measured data for the runs. For the Mach 7.16 case in Fig. 14, the Spalart–Allmaras model captures the data accurately. In Fig. 13, the over-prediction is somewhat larger at about 8 to 12%. The SST model performs the worst, predicting a level of turbulent heating in excess of the measurements by a nontrivial amount of approximately 20 to 30%. Here, we consider only cases for the HIFiRE trajectory nominal conditions near Mach 7, but measurements made on other test articles at higher Mach number conditions have shown some cases where the error in the predictions by the turbulence models become even worse at higher speeds.

The details of the transition and overshoot region also deserve some further consideration. Here, the production terms of the turbulence models were activated at the approximate onset position and allowed to build naturally. For these conditions, they build to an equilibrium turbulent level almost immediately, which does not adequately capture the transition and overshoot regions of the flow. The comparisons here were primarily intended to evaluate the models only in the equilibrium turbulent region. However, other researchers have made attempts to model the entire detailed region, primarily through analytical or empirical relationships [41], low Reynolds number turbulence closures [42], or additional transport equations for some type of intermittency variable [43,44]. Additionally, DNS offers some hope of modeling the entire region in the future but is currently limited in problem size and Reynolds number. Such efforts are beyond the scope of this work.

In addition to the RANS comparisons, the approximate analytical method known as Van Driest II [45] (abbreviated VD-II) is shown in the comparisons in Figs. 13 and 14. When compared with the data, the Van Driest prediction, which uses an adjusted von Kármán equation to compute the skin friction coefficient and a Reynolds analogy to estimate heat transfer, performs better than the RANS models. The Van Driest curves use the origin of the sharp-tipped cone to compute the skin friction value (and hence the heat transfer).

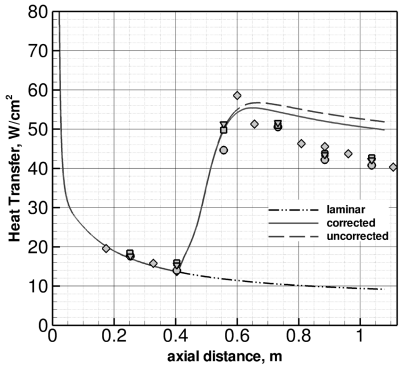

Fig. 15 Effect of correction for cold-wall compressible boundary-layer flow with SST Model for 2.5-mm nose for condition B (Mach 7.16, run 5).

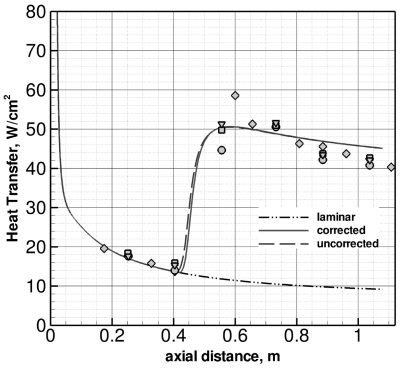

Fig. 16 Effect of correction for cold-wall compressible boundary-layer flow with Spalart–Allmaras model for 2.5-mm nose for condition B (Mach 7.16, run 5).

Although some researchers use other origins such as the average between the sharp- and the blunt-tip positions, Holden [46] showed that the sharp-tip origin works well for a surprisingly large range of flow conditions, even with appreciable bluntness to the shape. There was no correction applied due to the region of laminar flow at the front, because Holden's result showed again that the correlation seems to work well in the equilibrium turbulence region without such a laminar correction.

This result was investigated further to determine the source of the discrepancies between it and the RANS results. The key to the performance of the Van Driest method is in the selection of the Reynolds analogy law. As both Holden [46] and Goyne et al. [47] among others clearly show, this is a complex question and is dependent on the wall-to-total-temperature ratio. The commonly used form of the Reynolds analogy is shown in Eq. (1):

$$C_H = \frac{C_F}{2}\,\mathrm{Pr}^n \tag{1}$$

Here, the factor for the Prandtl number n is usually taken as $-\frac{2}{3}$, but those authors have shown that this factor reduces to zero (no Prandtl-number-factor dependency) for very cold walls. In both of the referenced experimental studies, skin friction as well as heat transfer were directly measured, and the plot of measured values of Eq. (1) as a function of wall-to-total-temperature (or enthalpy) shows this very clear trend (e.g., see Fig. 6 of [46] or Fig. 15 of [47]).

Because the cold-wall performance of the turbulence models is questionable, the effect of compressibility on the models was further examined. As proven by Huang et al. [48], extension of the transport-equation framework of the RANS models necessarily implies that the closure coefficients of a generic turbulent-transport equation must be a function of density gradients to reproduce the law of the wall. For a cold-wall boundary layer, density gradients are very large at the wall as they are driven by the thermal boundary layer. These results show that, because of the combinations of closure coefficients chosen, k-ε-based models will show the greatest influence from density gradients whereas k-ω-based models will have only a minimal influence. We also note that the SST model is a hybrid model that blends from a k-ω formulation at the wall to a k-ε formulation outside the boundary layer. Thus, the SST model should behave as a k-ω model in this case.

Catris and Aupoix [24] have implemented a proposed correction to several commonly employed RANS models that adjusts the diffusion terms to account for this dependency. Thus, the closure coefficients remain the same and the density gradient effect is included implicitly. The solution with the SST model with and without the Catris and Aupoix correction is shown in Fig. 15. As we expected from Huang et al. [48] analysis, the effect of the correction is small but does push the heating trend in the right direction. However, even with this adjustment to the model, heating is still somewhat overpredicted. The correction is part of the answer, but some additional problems with the prediction remain. The Spalart–Allmaras model, which performed somewhat better than SST for this case, is shown in Fig. 16 with and without the compressibility correction modification. Here, the effect on the heat transfer is negligible. A comparison of typical profiles on the forebody showed that there were some changes to the overall transport-variable profile (so we know that the modification is working), but the effect in the near-wall region was minimal. Even without the correction, we note that the Spalart–Allmaras model performs reasonably well at this Mach number. Although the effects of compressibility on the law of the wall are important to consider, in this case we must conclude that additional issues must be considered in computing the turbulent heating for this simple flowfield.

The HIFiRE test conditions are fully duplicated flight enthalpy of 2.5 MJ/kg for Mach 7 and the wall is an isothermal 300 K surface, and so the total-to-wall-temperature ratio is about 0.1 for these tests. Some additional data are available at fully duplicated Mach 10 conditions with the same geometry (though longer in total length). In that case, with a total enthalpy of almost 5 MJ/kg, the wall-to-total-temperature ratio is 0.06. The turbulent predictions with the three RANS models are shown for both the Mach 7 and 10 conditions in

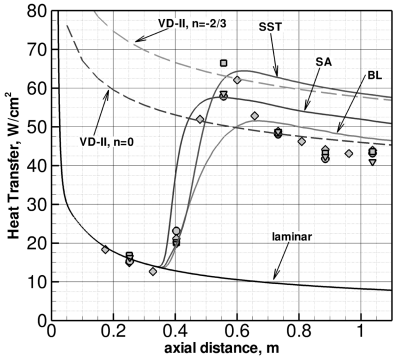

a) Mach 6.58, run 4

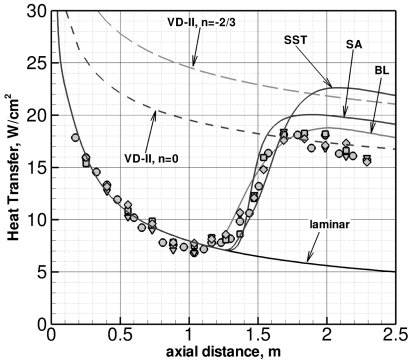

b) Mach 9.95, run 19

Fig. 17 Comparison of two different Reynolds analogy factors and RANS turbulence model predictions for cone heating (Mach 7 and 10).

Fig. 17. This figure compares the data to the Van Driest II model computed two ways, first with a Prandtl-number factor of $n = -\frac{2}{3}$ and then with $n = 0$. Based on the data of Holden [46] and Goyne et al. [47] in this regime we expect the $n = 0$ case to better predict the measured heating. For the Mach 10 condition, the qualitative result is the same as it was for Mach 7 where the Van Driest II law with a properly selected Reynolds analogy outperforms the CFD RANS models. However, the commonality in these two cases is that the Baldwin–Lomax model predicts heating that coincides closely with the $n = 0$ version of Van Driest II. This is consistent with why it was judged to predict the measured heating the best out of the three models. In both cases, however, the SST model coincides very closely with the $n = -\frac{2}{3}$ version of Van Driest II. This does not seem to be a coincidence when one considers that the SST model was calibrated for transonic flows (with total-to-wall-temperature ratios of near 1.0) and has been adapted to hypersonic flows with the set of calibration coefficients unmodified. As noted by Goyne et al. [47], both the $n = -\frac{2}{3}$ version of Van Driest II and the SST model closely reproduce the linear form of the Crocco energy relation, which does not seem to hold as enthalpy increases.

The result suggests that for flows with total-to-wall-temperature ratios nearer to 1.0, the SST model may predict the heating more accurately. However, for higher enthalpy flight conditions than we have considered for the HIFiRE-1 vehicle, the total-to-wall-temperature ratio must become very large. Although the Baldwin–Lomax model provides an equitable solution for this case, it has severe limitations in adverse pressure gradient flows and in complex three-dimensional flows typical of vehicles at an angle of attack, and so improvements to the transport-level models must be made to handle more general flows. The database to understand the dependency of turbulent heating for cold walls is very sparse, and a more thorough experimental study is required to fully understand the physics of the situation.

VII. Comparison of Turbulent Midbody Heating Calculations to Experiment

The turbulent heating predictions on the cylindrical midbody are also of interest in the computation of the HIFiRE-1 flowfield. For the purpose of the ground test and the CFD simulations presented here, we are principally concerned only with the potential relaminarization that could occur from the expansion onto the cylinder. This is important to the flare interaction experiment because we need to understand the state of the boundary layer entering the interaction region. The capability to predict the level of turbulent heating on the midbody is generally related to the prediction on the forebody as shown in the previous section.

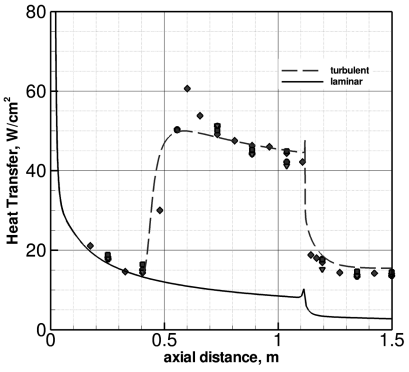

Fig. 18 Comparison of cylindrical midbody heating to laminar and turbulent predictions for test condition B (Mach 7.16).

A typical comparison for the midbody heating is shown in Fig. 18, which compares fully laminar and turbulent solutions using the Spalart–Allmaras model to the data for run 14 at test condition B. By comparing directly with the CFD solution, we observe that the drop in heating from the corner expansion is close to the decrease in heat transfer that is predicted by the CFD solution for a fully turbulent boundary layer. Although the results from the previous section called somewhat into question the capability of the RANS models to accurately predict this heating level, the measured data level is considerably above where we would expect the level to be if the boundary layer had returned to an equilibrium laminar condition. We saw this behavior consistently in all cases except for one case at a very low Reynolds number (run 31). Thus, our test series for this configuration seems to indicate that the turbulent boundary layer is very robust and provides a fully turbulent boundary-layer entry condition to the flare interaction region along the trajectory regime.

VIII. Comparison of Turbulent Interaction Region Calculations to Instrumented Flare Experiment

Finally, the modeling of the shock/turbulent boundary layer interaction region on the flare is reviewed. The experiment studied four different flare angles, including 27, 30, 33, and 37 deg, where 37 deg was the pretest design angle provided to CUBRC for the phase I design. Schlieren images are available for all configurations, though only the 33 deg flare was selected to be instrumented with heat transfer and pressure gages for the phase II runs. For these cases several turbulence models have been evaluated and compared with the available data, both visual and quantitative. The experiment studied the flare configuration at various angles of attack, but we have restricted comparison here to the cases at 0 deg for ease of computation. The experimental results indicated that the physical mechanisms governing the interaction region structure would be similar within the range of angle of attack up to 5 deg studied in the experiment [1]. For all the cases considered in this work, the Schlieren movies from the experiment showed the shock system and the separation zone size to be constant for the entire run, and no significant fluctuations were observed. The only condition that showed a fluctuating separation region was the condition at a very low Reynolds number where the incoming boundary layer on the cylinder did not appear to be fully turbulent and the fluctuations were presumed to be a manifestation of the transitional state of the driving boundary layer. That condition is not considered further in this work. The RANS solutions can be compared with a single representative frame of the high-speed movie for the remaining runs.The comparison of the separated region predicted for the Mach 7.16 condition is shown for the 33 deg flare from phase I in Fig. 19 for the SST and Spalart–Allmaras turbulence models. The Schlieren image from the experiment illustrates the dramatic disagreement with the conventional RANS models. The experiment shows a separated region on the order of the length of the flare. In the case of the Spalart–Allmaras model, no separation zone is predicted at these conditions. For the SST model, in contrast, the separated region size is predicted to be more than twice as big as in the experiment. The comparison is shown quantitatively in Fig. 20 by plotting the shear stress value on the surface, where a zero value locates the separation point. The separation point from the experiment is estimated from the

Fig. 19 Comparison of predicted and measured separation zone flowfield on 33 deg flare at condition B (Mach 7.16, all images shown approximately equal scale).

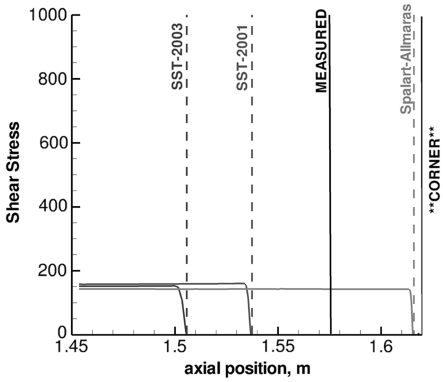

Fig. 20 Comparison of shear stress distribution showing predicted and measured separation point on 33 deg flare for condition B (Mach 7.16).

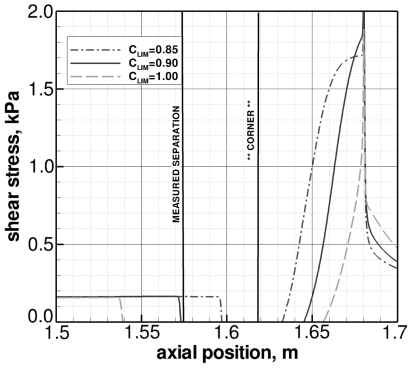

Fig. 21 Comparison of shear stress distribution showing predicted and measured separation point on 33 deg flare for condition B (Mach 7.16) using SST modified stress limiter form.

location of the separation shock. Although this method is not as accurate as distributions of pressure, heat transfer, or (ideally) skin friction [49], it allows for a qualitative assessment of the CFD modeling using the available data. As corroborated by the Schlieren images, the Spalart–Allmaras model predicts nearly zero separation as the shear stress goes to zero approximately at the corner. The two SST solutions shown have been computed with (SST2003) and without (SST2001) the spreading rate compressibility correction included in the model. This compressibility correction is a Sarkar et al. [50] type of turbulent Mach number correction to the production term designed to improve the agreement with spreading rates in high speed mixing layers. Brown [23] has adapted this type of correction to the SST model by incorporating a switch that shuts off the influence of the correction near the wall and prevents it from distorting the law of the wall in attached boundary layers. However, the compressibility correction has a significant negative effect on the prediction of the separated region size, increasing the error from 2.0 times to 2.75 times the experimental value. The adverse effect of the Sarkar correction on this type of flow has been demonstrated before, but even absent the correction's influence the predictions are still very poor for all models.

From these predictions using the basic models, the results are discouraging. The work from the previous sections indicates that there are significant challenges in predicting even cold-wall attached heating correctly. On the attached cone, analysis indicated that an algebraic or analytical model could be employed to predict the heating pattern. Here in the flare region, however, those models have no validity, and the partial-differential-equation-based models seem to do a little better. In the case of the SST model, the source of this discrepancy can be traced to the predicted increase in Reynolds shear stress (i.e., eddy viscosity for RANS models) caused by the vorticity from the separation shock. This is exactly the behavior discussed by Wilcox [51] (p. 282), who describes that the tendency to predict far too large a separation zone is related to the overly aggressive choice of stress-limiting in the SST model. Fortunately, this behavior can be controlled, and a different choice of Reynolds stress limiter in a model like the Wilcox-2006 k-ω can be expected to predict a separation zone size much closer to the experiment. Similarly, it is straightforward to apply Wilcox's type of stress limiting to the SST model by adjusting the coefficient in the eddy viscosity computation. The definition of eddy viscosity for the SST model is defined in Eq. (2), where the coefficient is typically implied.

$$\mu_T = \frac{\rho k}{\max[\omega, C_{\mathrm{LIM}}\Omega F_2/0.31]} \tag{2}$$

By adjusting the value of the coefficient C_{LIM} in the model, the separation region may be altered. The value in the nominal SST model is 1.0, which is too large. Reducing this value produces a smaller separated region. Shown in Fig. 21 is the predicted shear stress pattern for several values of C_{LIM} illustrating separation and reattachment point compared with the same run 14 experiment. For our cases, a value of 0.90 seems about right, which is reasonably consistent with Wilcox's recommended value of 0.875 for his model. After making this adjustment to the model, the predicted flowfield using the new SST model is overlayed with the experimental Schlieren in Fig. 22 for this case. As the figure shows, the agreement with the flowfield structure and shock pattern is excellent. A study by Edwards et al. [52] on a Mach 5 compression corner with large eddy simulation and RANS models found agreement with a value of 0.90 also, which provides some confidence that this modification may hold for a wide range of flow conditions and is not particular to this case. Additional tests in very different flow regimes are needed to determine if a constant value is sufficient or if C_{LIM} should be a function of the flow variables in some way.

The understanding that the prediction of the rise in the Reynolds shear stress downstream of separation is the cause of the issues in predicting the size of the separation zone means that the Spalart–Allmaras model can be modified in a similar way to improve its predictive capability for this flow. For the SA model, eddy viscosity production is a simple source term proportional to an effective vorticity with a calibrated coefficient, C_{b1}. From the original SA specification, C_{b1} is 0.1355 and has been used by default in DPLR's hypersonic version of the model. From Figs. 19 and 20 we recognize that too much eddy viscosity is being produced, causing the separation zone size to shrink to almost nothing.

A modification to the SA model production term exists and is called strain-adaptive linear Spalart–Allmaras [53] (SALSA). The model is a heuristic modification to the C_{b1} coefficient, the primary effect of which is to limit the production in regions of excessive strain. Like the Wilcox limiter in SST, the SALSA modification is easy to implement in the existing code by computing a new value of C_{b1}. The modified coefficient is defined in Eqs. (3–6).

$$\alpha_1 = \left[1.01\left(\frac{\tilde{\nu}}{\kappa^2 d^2 S}\right)\right]^{0.65} \tag{3}$$

Fig. 22 Comparison of measured and predicted flowfield structure on 33 deg flare for condition B (Mach 7.16) using modified stress limiter form with coefficient $C_{\mathrm{LIM}} = 0.90$.

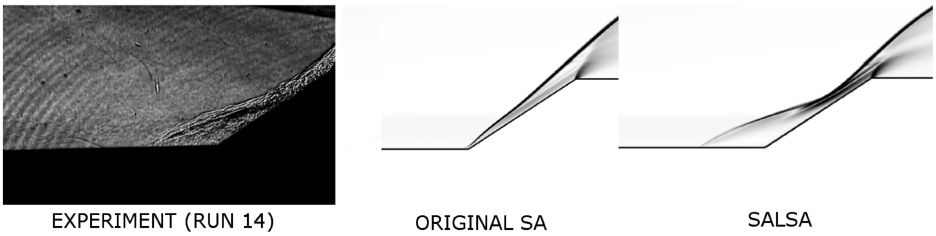

Fig. 23 Comparison of predicted and measured separation zone flowfield on 33 deg flare for condition B (Mach 7.16) using SALSA [53] modification to SA model (all images shown approximately equal scale).

$$\alpha_2 = \max\left\{0, \left[1 - \tanh\left(\frac{\tilde{\nu}}{68\nu}\right)\right]^{0.65}\right\} \tag{4}$$

$$\Gamma = \min[1.25, \max(\alpha_1, \alpha_2, 0.75)] \tag{5}$$

$$C_{b1} = 0.1355\sqrt{\Gamma} \tag{6}$$

This modification has been tested on run 14, and the comparison to the experiment and the original result is shown in Fig. 23. The effect is immediately obvious and improves the separation zone size and structure dramatically, just as the limiter change did with SST. As with the SST modification, the SALSA modification employs tunable coefficients that can be easily adjusted to change the strength of the Reynolds stress limitation, but the nominal values recommended by Rung et al. [53] seem to be reasonable for this application also. Therefore, additional adjustment has not been performed. It is also interesting to note that this correction has been used with the simple RANS version of Spalart–Allmaras to improve the agreement with the experiment. Recent advances in coupling detached eddy simulation to the Spalart–Allmaras model have shown dramatically different performance in massively separated regions [54]. It is unknown what effect the SALSA modification would have if used in conjunction with detached eddy simulation, but would be an interesting future study.

The modifications of these models to improve the prediction of separated region structure led to an important adjustment to the phase II model. Although the separation zone size determined from the Schlieren images in phase I and the modified RANS model predictions show a separated region of the order of the length of the flare and demonstrate reattachment on the flare face, the reattached boundary layer on the flare has not reached an equilibrium state before the corner for this condition. For this reason, as described by Wadhams et al. [1], it was decided to increase the length of the flare in the ground test in order to provide better data to calibrate the turbulence models quantitatively for flight vehicle design. The lengthened flare, which corresponds to the 409 mm diam in Fig. 4, was modeled using the stress-limited SST model and compared with the original phase I flare. The comparison of predicted surface pressure for the two geometries is shown in Fig. 24. The flow on the short flare reattaches but extends only just aft of the peak reattachment compression. The flow on the longer flare asymptotes to the cone pressure value before expanding around the corner to the outer surface, creating a more robust code validation exercise because the predicted cone pressure can be compared with the experiment. We also note that the size and character of the separation is the same for both configurations because the flow has reattached even on the shorter flare. This behavior was confirmed by the experiment in the early phase II runs.

Quantitative comparisons can be made using data from the instrumented flare section from phase II, where distributions of heat transfer and pressure were measured for a distance upstream of the flare and on the flare itself. The heat transfer is the most sensitive metric of comparison. As shown in Fig. 25, the surface pressure and heating distributions measured for run 36 at condition B is plotted with the predictions for the original (unmodified) SST model, and the version with the modified stress limiter is set at 0.90. As was shown

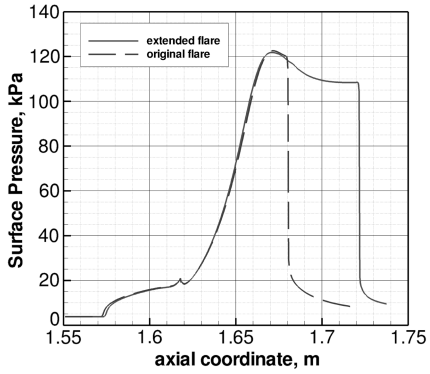

Fig. 24 Comparison of surface pressure profile for original and extended flare configurations predicted by modified SST model.

qualitatively for the phase I tests, the original SST model predicts far too large a separated region whereas the modified model predicts the structure of the flow much more accurately. Even for the modified solution, agreement is not perfect. The reattachment peak pressure is somewhat underpredicted and the peak heat transfer overpredicted.

The reason for the disagreement in pressure was disconcerting at first, but further consideration by the authors revealed some qualitative observations. If the separation over the flare is simply considered as the summation of two turns, one through the separation shock and a second onto the flare itself, we observe that the pressure rise predicted by the modified SST model at the separation shock is slightly too steep. This implies that to conserve the total turning imposed by the flare geometry the second increment is slightly too gentle. These discrepancies are small in each instance, but even small differences can have a large effect on the recovered pressure. We also note that it is not clear if the overprediction in heat transfer on the flare face is due to this same logic or if the overprediction is simply consistent with the behavior that was observed on the conic forebody. However, as it is, the modified SST model performs much better than the original model does in both a qualitative and a quantitative sense. When one considers the purpose of such calculations, the quantitative agreement with the data is probably sufficient for a first-order design level calculation to design the flight experiment.

Similarly, the solution predicted by the Spalart–Allmaras model with and without the SALSA modification is shown in Fig. 26. Here again, the modification to improve shock interaction performance does significantly improve the model's performance. As we saw earlier, without modification the model predicts no separated region and fails utterly to predict the surface pressure and/or heating in the flare region. The SALSA modification, using the coefficients recommended by the original authors, improves the overall character of the separated region. Given the empirical nature of this calculation, it is obvious that one could further improve the agreement with the separated region size by adjusting the coefficients somewhat, but the recommended values are a reasonable starting approximation. The primary limitation here is in the prediction of the heat transfer, which is considerably poorer in the reattachment region than the two-equation model. In this aspect, the SST model fares considerably better in that it showed a smooth increase in heating through the reattachment compression process to the peak that

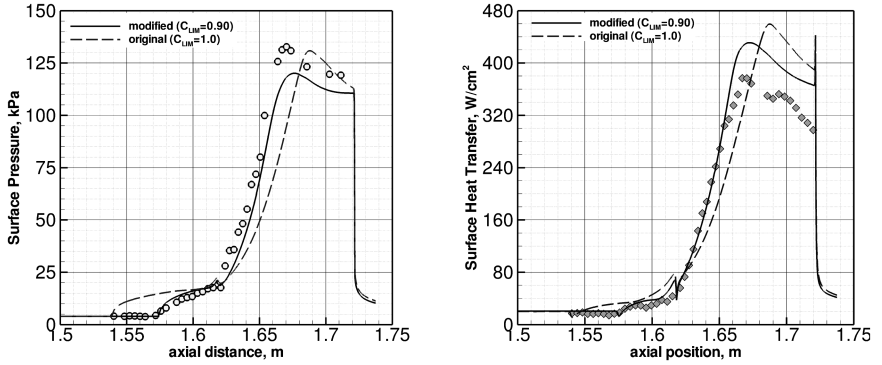

a) Surface pressure b) Surface heat transfer

Fig. 25 Comparison of measured surface pressure and heat transfer on flare for run 36 with original and modified SST prediction.

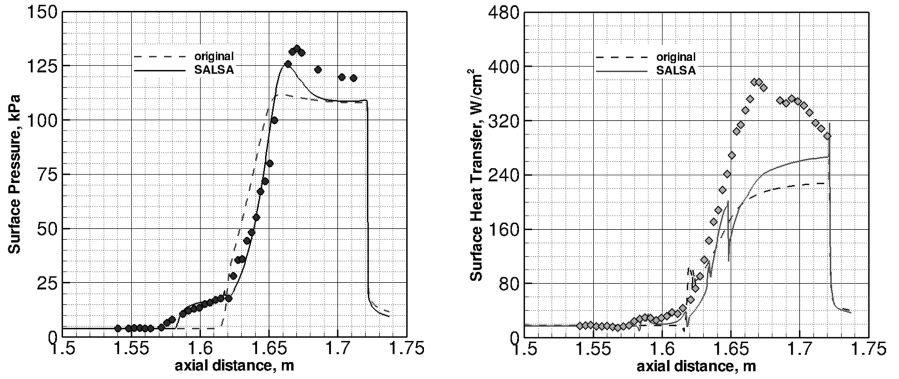

a) Surface pressure b) Surface heat transfer

Fig. 26 Comparison of measured surface pressure and heat transfer on flare for run 36 with original and modified Spalart–Allmaras prediction.

matched the experimental data very closely. The Spalart–Allmaras model, even with the SALSA modification, is disrupted in this region. Still, because it was shown that the Spalart–Allmaras model was in better general agreement on the attached forebody section of the vehicle than SST, it remains a useful model for design level calculations on the flight vehicle.

Finally, with a set of calibrated tools available for flight vehicle design, the full tip-to-tail flight vehicle configuration was computed at 0 deg angle of attack with a radiative equilibrium wall boundary. The SST model with the modified stress limiter was selected to compute this flow because it was found to generally perform the best in this region. The transition-onset point of the flow was taken from Fig. 12 as 0.65 m based on the STABL analysis of the hot-wall flight condition and assuming a median N factor of 9.5. The computed flowfield and pressure distribution for this flight condition is shown in Figs. 27 and 28. In flight, the flare is equivalent to the short flare from the ground test and can be compared with the run 14 results and predictions shown in Fig. 22 and pressure and heating measurements up to a station of $X = 1.68$ m in Fig. 25. The hotter wall of the flight case is predicted to have only a small impact on the flare structure, which, as in the ground test, just reattaches on the flare and reaches the peak compression before expanding around the corner. Thus, we note that the ground test was a good simulation on the flight despite differences in the surface temperature.

The effect of the transition-onset location was also considered for this radiative equilibrium flight vehicle configuration by arbitrarily assuming transition to take place immediately downstream of the nosetip rather than back on the forebody as predicted by the STABL code. This comparison is shown between the two transition-onset locations in Fig. 28. The difference in the predicted separation zone size that is observed may be thought of, to first-order, as a function of the incoming boundary-layer thickness, which changes depending on the running length of turbulent flow upstream of the flare. Therefore, it is critical to the calculation to estimate the approximate boundary-layer transition-onset location with the STABL code to design the flare accurately. This result underscores the need to employ the calibrated tools in an integrated way and shows that both

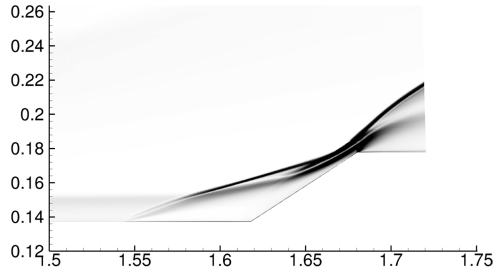

Fig. 27 Computational Schlieren of predicted flowfield on the flare for flight vehicle at trajectory condition B using modified SST model.

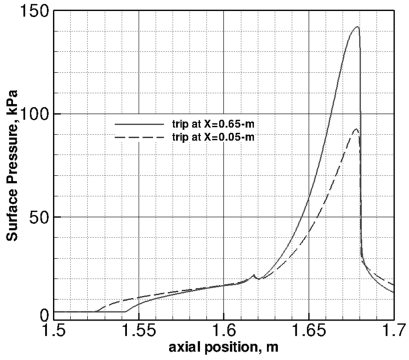

Fig. 28 Effect of transition-onset location on flare separation region size for flight vehicle at trajectory condition B using modified SST model.

the DPLR code and the STABL code contribute to flight vehicle design.

IX. Numerical Accuracy

In accordance with the AIAA policy on uncertainty in numerical methods [55], the accuracy of the CFD simulations are addressed. The uncertainties and accuracy of the experimental data are addressed separately [1], and so we will assume that the experimental data are nominally accurate for our purposes here. To address the uncertainty in the CFD simulation, ordered discretization error is the primary source of error. The DPLR code converges rapidly because of the line-relaxation method, and so the convergence error is typically negligible. Simulations in this study were converged to about 10 orders of magnitude of residual decrease, although experience has shown that this is more than is required. Simulations with the flare interaction region where the level of residual decrease is limited by ringing of the separation zone were monitored until the size of the separation zone and surface heating level stopped changing. An example of this convergence behavior is shown in Fig. 29, which plots the axial position of the separation point ahead of the flare for the case with the SST model using the modified limiter. This position was found by the position where the surface shear stress becomes zero. The DPLR method is a first-order, global time-stepping method, and so the flow evolves uniformly. By 8 ms of flow evolution time (initializing from freestream conditions) the position of the separation point has converged to six decimal places and the shock system does not move further. An interesting study by Sinha et al. [56] assessed the effect of shock unsteadiness on the prediction of turbulent shock interaction regions with RANS models. They noted that one of the major implications of shock unsteadiness is to limit the production of turbulent shear stress through the shock, which is exactly what the modification studied here does in an averaged sense.

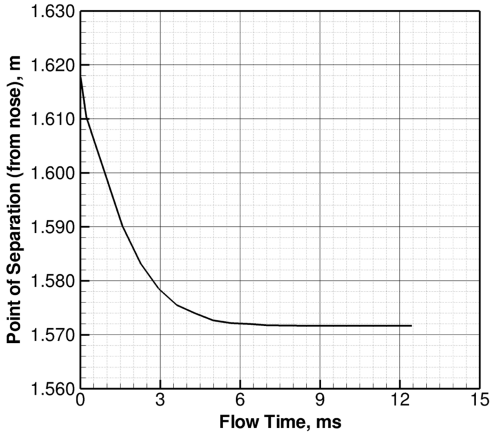

Fig. 29 Convergence history of flow separation point.

The run 4 case was used as a typical measure of ordered discretization error. A grid of 832×512 grid points was used as the finest grid with cell Reynolds number values of nominally 0.50 to the first cell center. This grid was sequenced several times by removing every other grid point to form grids 416×256 and 208×128. For the mean flow analyses given in this study, grids similar to the finest and/or second finest grid were employed. The results for laminar forebody heating as well as turbulent heating predictions with each of the three RANS models are shown in Figs. 30a–30d. For the laminar flow, the three grids are converged to better than 0.1%. The Spalart–Allmaras solutions converged to better than 0.3% and the Baldwin–Lomax solutions converged to better than 0.5% at all stations. The SST model shows the greatest sensitivity to grid resolution, where the coarsest grid displays differences of up to 2.2%. However, the two finest grids, representative of the density of cells used in the study, agree within 0.7%. For second order convergence, the Richardson extrapolation error estimator is equal to one-third of these percent difference values. This behavior can be reduced below second order in the presence of shocks, but we can conservatively estimate that the simulations performed in previous sections should be accurate to within 1% for the laminar and turbulent mean flow forebody.

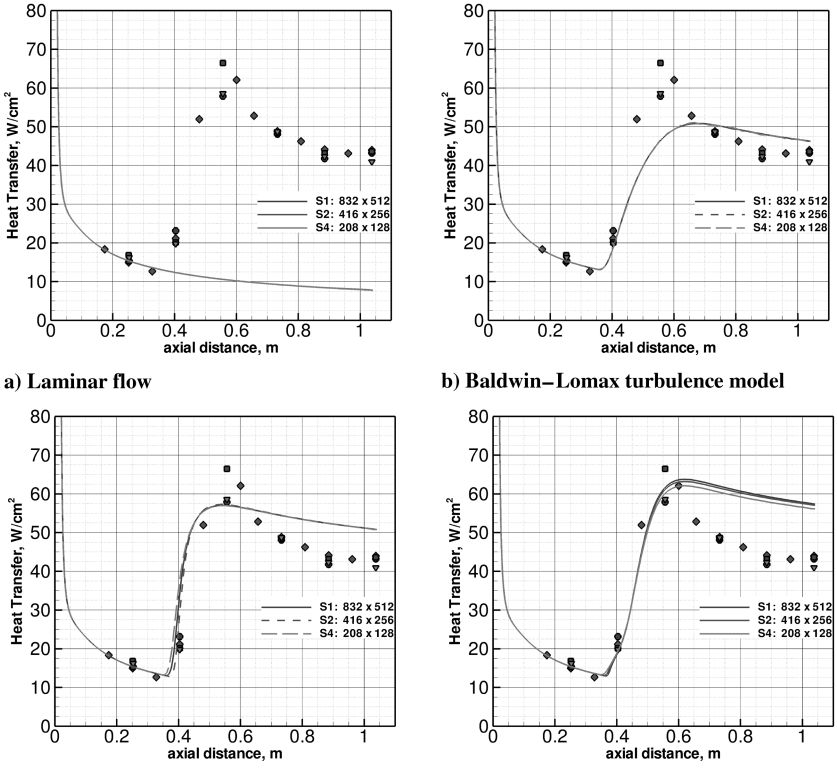

a) Laminar flow **b) Baldwin–Lomax turbulence model**

c) Spalart–Allmaras turbulence model **d) SST turbulence model**

Fig. 30 Grid convergence study for run 4 for laminar and RANS turbulent prediction.

The behavior of the stability code with respect to grid resolution is a separate matter and is slightly more complex because it depends on the quality of the mean flow solution as well as the density of points tested by the PSE solver. Therefore, ordered discretization was considered in two forms. First, the laminar mean flow solution sequences considered previously were used with a common test map of 1482 points. This result is shown in Fig. 31a. The results were pleasantly surprising in that the predicted N-factor distribution for the three-sequence grid differed by less than 1% over the entire body. Because the simulation was found to be so consistent with respect to mean flow resolution, the grid was sequenced one more time to produce 108×64 cells. With this very crude grid, the boundary layer was defined by as few as 25 points at certain stations but the amplitude growth N factor deviated from the finest result by no more than 3%. This is still an acceptable uncertainty for the prediction of transition. This analysis provided significant confidence in the consistency of the STABL code. Although we continue to recommend that the stability analysis be performed with a minimum of 100 points defining the boundary layer, this shows that the PSE solver can generate good solutions with even much cruder mean flow results. The sensitivity to the resolution of the test map was also considered by doubling the number of both frequencies and starting locations of instabilities in the test grid for the 416×256 mesh so that a total of 5928 points were tested. The comparison is shown in Fig. 31b. As we have found previously in this type of study [37], increasing the number of points smooths out the envelope somewhat by filling in the valleys more evenly. However, the trend line defined by the peaks of the instabilities is unchanged, and the increased number of points results in only a cosmetic improvement to the solution. Thus, we would not expect the number of test map points selected for the STABL solution to alter our engineering determination of the transition point at all.

Finally, ordered discretization error was considered for the flare interaction region. Because of the complex block topology used for this part of the analysis, a strict grid sequencing was not possible. However, a coarser grid with less than half of the number of grid cells in the interaction region was compared with the original. This is shown in Fig. 32, which compares the pressure and heat transfer predictions for both grids using the modified (stress-limited) SST model. Generally, the solutions are compatible with the largest differences appearing postattachment where the boundary layer is thin. We find an error of no more than 2% in predicted pressure and 3% in predicted heat transfer for the flare interaction region.

X. Conclusions

Two series of full-scale, fully duplicated ground tests have been performed on the HIFiRE-1 flight vehicle geometry in the CUBRC LENS I facility. The primary goal of this experimental test program has been to design several critical aspects of the flight vehicle such as nose radius, flare sizing, and trip specification. The secondary goal of the ground test is to do direct comparison to flight test data if a successful flight occurs. Until such a time as the flight data become available, however, the ground test data provide a valuable resource with which to evaluate and tune our numerical methodologies to validate computational predictions.

With regard to the forebody natural transition process governed by second-mode instability, this and other studies [37,38] have shown that the STABL tool provides a good prediction of the transition-onset process. In this particular nozzle, the amplitude growth based on an e^N correlation resulted in N factors ranging from 4.9 to 6.8 with an average of 5.7. Scaling the ground test data to flight results in a potential delay of transition onset of up to 20-cm on the 1.1 m untripped, smooth forebody, which still provides laminar, transitional, and turbulent heating on the forebody cone for these conditions.

Comparisons with turbulent forebody heat transfer predictions using several RANS models revealed a surprising range of solutions for a straightforward geometry. By comparing the RANS solutions,

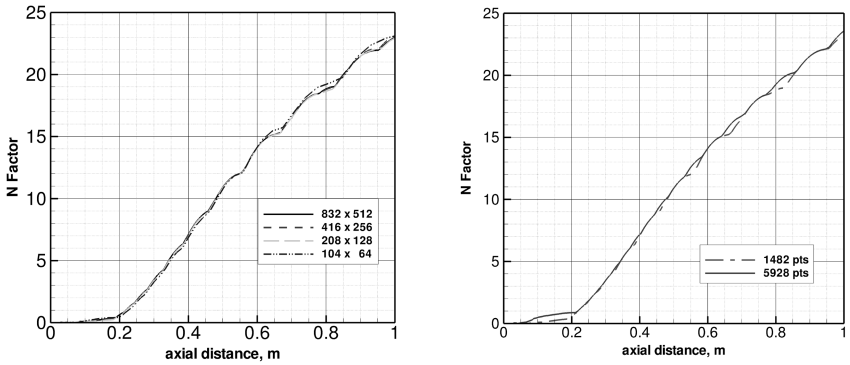

a) Sensitivity to mean flow resolution b) Sensitivity to test map resolution

Fig. 31 Study of grid convergence and test point matrix convergence of STABL solution for run 4.

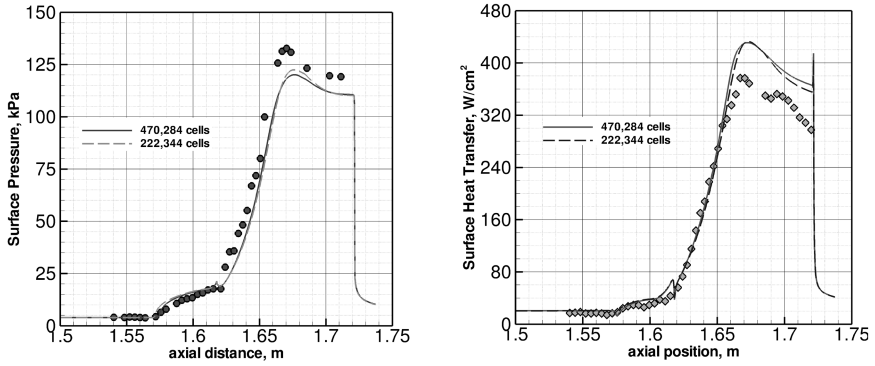

a) Surface pressure b) Surface heat transfer

Fig. 32 Grid convergence study for run 36 flare region computation.

which tended to predict an excess of turbulent heating compared with the experimental data, vs predictions using the Van Driest II method, it was observed that the correlation between skin friction and heat transfer is dependent on the wall-to-total-temperature ratio in the flow. Initial observations suggest that the SST model in particular might perform better for ratios closer to 1.0 than for these tests. However, as vehicle speed increases and high temperature ratios become infeasible, this issue remains a primary challenge to vehicle design and needs to be addressed further.

Finally, results comparing with the flare interaction region have shown that two of the most commonly employed RANS models, shear stress transport and Spalart–Allmaras, perform poorly in predicting the flowfield structure in their native form. A rapid increase in Reynolds stress caused by the separation shock is the dominant driver of the size of the interaction region, and simple modifications that control (or limit) how rapidly the Reynolds stress is allowed to grow can dramatically improve the agreement with the experimental data. There are many approaches to this basic philosophy of controlling the Reynolds stress in shock-separated regions, but the modifications reviewed here are emphasized because of their simplicity such that they can be integrated into the existing RANS models with only a few lines of code.

In summary, we have shown that the methodologies used here might successfully be employed to perform design level calculations of a HIFiRE flight vehicle. Particularly with the turbulence models, however, we emphasize that a wide variety of solutions can be obtained using accepted models and that the ground test database must be employed to sensibly calibrate the models to provide reasonable flight calculations. We have provided results demonstrating the influences on the prediction techniques and demonstrated one possible set of tools available to designers.

References

[1] Wadhams, T., MacLean, M., Holden, M., and Mundy, E., "Ground Test Studies of the HIFiRE-1 Transition Experiment Part 1: Experimental Results," *Journal of Spacecraft and Rockets*, Vol. 45, No. 6, 2008, pp. 1134–1148.

[2] Kimmel, R., Adamczak, D., Gaitonde, D., Rougeux, A., and Hayes, J., "HIFiRE-1 Boundary Layer Transition Experiment Design," *45th Aerospace Sciences Meeting & Exhibit*, AIAA Paper 2007-0534, Jan. 2007.

[3] Holden, M. S., and Parker, R. P., "LENS Hypervelocity Tunnels and Application to Vehicle Testing at Duplicated Flight Conditions," *Advanced Hypersonic Test Facilities*, edited by F. K. Lu, and D. E. Marren, Vol. 198, AIAA Progress in Astronautics and Aeronautics Series, AIAA, Reston, VA, 2002, Chap. 4.

[4] Holden, M. S., Wadhams, T. P., and Candler, G. V., "Experimental Studies in the LENS Shock Tunnel and Expansion Tunnel to Examine Real-Gas Effects in Hypervelocity Flows," AIAA Paper 2004-0916, Jan. 2004.

[5] Parker, R., Wakeman, T., Holden, M., and MacLean, M., "Measuring NO Freestream Concentration Using Quantum Cascade Lasers at CUBRC," *44th Aerospace Sciences Meeting & Exhibit*, AIAA Paper 2006-0926, Jan. 2006.

[6] Parker, R., Wakeman, T., MacLean, M., and Holden, M., "Measuring Nitric Oxide Freestream Velocity Using Quantum Cascade Lasers at CUBRC," *45th Aerospace Sciences Meeting & Exhibit*, AIAA Paper 2007–1329, Jan. 2007.

[7] Wright, M. J., Bose, D., and Candler, G. V., "A Data Parallel Line Relaxation Method for the Navier–Stokes Equations," *AIAA Journal*, Vol. 36, No. 9, Sept. 1998, pp. 1603–1609. doi:10.2514/2.586

[8] MacCormack, R. W., and Candler, G. V., "The Solution of the Navier–Stokes Equations Using Gauss–Seidel Line Relaxation," *Computers and Fluids*, Vol. 17, No. 1, 1989, pp. 135–150. doi:10.1016/0045-7930(89)90012-1

[9] Candler, G. V., "Chemistry of External Flows," *Aerothermochemistry for Hypersonic Technology*, Von Karman Institute for Fluid Dynamics Lecture Series, Vol. 1995-04, Von Karman Institute for Fluid Dynamics, Rhode-St-Genese, Belgium, April 1995.

[10] Landau, L., and Teller, E., "Theory of Sound Dispersion," *Physikalische Zeitschrift der Sowjetunion*, Vol. 10, No. 34, 1936, pp. 34–43.

[11] Millikan, R., and White, D., "Systematics of Vibrational Relaxation," *Journal of Chemical Physics*, Vol. 39, No. 12, 1963, pp. 3209–3213. doi:10.1063/1.1734182

[12] Camac, M., "CO_2 Relaxation Processes in Shock Waves," *Fundamental Phenomena in Hypersonic Flow*, edited by J. G. Hall, Cornell University Press, Ithaca, NY, 1964, pp. 195–215.

[13] Park, C., Howe, J. T., Jaffe, R. J., and Candler, G. V., "Review of Chemical-Kinetic Problems of Future NASA Missions II: Mars Entries," *Journal of Thermophysics and Heat Transfer*, Vol. 8, No. 1, 1994, pp. 9–23. doi:10.2514/3.496

[14] Park, C., "Assessment of Two-Temperature Kinetic Model for Ionizing Air," *AIAA 22nd Thermophysics Conference*, AIAA Paper 87-1574, June 1987.

[15] Marrone, P. V., and Treanor, C. E., "Chemical Relaxation with Preferential Dissociation from Excited Vibrational Levels," *The Physics of Fluids*, Vol. 6, No. 9, Sept. 1963, pp. 1215–1221. doi:10.1063/1.1706888

[16] Palmer, G. E., and Wright, M. J., "A Comparison of Methods to Compute High Temperature Gas Viscosity," *Journal of Thermophysics and Heat Transfer*, Vol. 17, No. 2, 2003, pp. 232–239. doi:10.2514/2.6756

[17] Palmer, G. E., and Wright, M. J., "A Comparison of Methods to Compute High Temperature Gas Thermal Conductivity," AIAA Paper 2003-3913, June 2003.

[18] Gupta, R., Yos, J., Thompson, R., and Lee, K., "A Review of Reaction Rates and Thermodynamic and Transport Properties for an 11-Species Air Model for Chemical and Thermal Nonequilibrium Calculations to 30000 K," NASA RP-1232, Aug. 1990.

[19] Ramshaw, J. D., "Self-Consistent Effective Binary Diffusion in Multicomponent Gas Mixtures," *Journal of Non-Equilibrium Thermodynamics*, Vol. 15, No. 3, 1990, pp. 295–300.

[20] Baldwin, B. S., and Lomax, H., "Thin Layer Approximation and Algebraic Model for Separated Turbulent Flows," AIAA Paper 78-0257, 1978.

[21] Spalart, P. R., and Allmaras, S. R., "A One-Equation Turbulence Model for Aerodynamic Flows," *30th Aerospace Sciences Meeting & Exhibit*, AIAA Paper 92-0439, Jan. 1992.

[22] Menter, F. R., "Two-Equation Eddy-Viscosity Turbulence Models for Engineering Applications," *AIAA Journal*, Vol. 32, No. 8, Aug. 1994, pp. 1598–1605. doi:10.2514/3.12149

[23] Brown, J., "Turbulence Model Validation for Hypersonic Flow," *8th Thermophysics and Heat Transfer Conference*, AIAA Paper 2002-3308, June 2002.

[24] Catris, S., and Aupoix, B., "Improved Turbulence Models for Compressible Boundary Layers," *2nd Theoretical Fluid Mechanics Meeting*, AIAA Paper 98-2696, June 1998.

[25] Saunders, D., Yoon, S., and Wright, M., "An Approach to Shock Envelope Grid Tailoring and Its Effect on Reentry Vehicle Solutions," *45th Aerospace Sciences Meeting & Exhibit*, AIAA Paper 2007-0207, Jan. 2007.

[26] Johnson, H. B., "Thermochemical Interactions in Hypersonic Boundary Layer Stability," Ph.D. Dissertation, Univ. of Minnesota, Minneapolis, MN, 2000.

[27] Johnson, H., and Candler, G., "Hypersonic Boundary Layer Stability Analysis Using PSE-Chem.," *35th AIAA Fluid Dynamics Conference and Exhibit*, AIAA Paper 2005-5023, June 2005.

[28] Johnson, H., and Candler, G., "Analysis of Laminar-Turbulent Transition in Hypersonic Flight Using PSE-Chem," *36th AIAA Fluid Dynamics Conference and Exhibit*, AIAA Paper 2006-3057, June 2006.

[29] Herbert, T., "Boundary Layer Transition–Analysis and Prediction Revisited," AIAA Paper 91-0737, Jan. 1991.

[30] Malik, M., "Prediction and Control of Transition in Superconic and Hypersonic Boundary Layers," *AIAA Journal*, Vol. 27, No. 11, Nov. 1989, pp. 1487–1493. doi:10.2514/3.10292

[31] Malik, M. R., "Hypersonic Flight Transition Data Analysis Using Parabolized Stability Equations with Chemistry Effects," *Journal of Spacecraft and Rockets*, Vol. 40, No. 3, May–June 2003, pp. 332–344. doi:10.2514/2.3968

[32] Jaffe, N. A., Okamura, T. T., and Smith, A. M. O., "Determination of Spatial Amplification Factors and Their Application to Predicting Transition," *AIAA Journal*, Vol. 8, No 2, Feb. 1970, pp. 301–308. doi:10.2514/3.5660

[33] Stilla, J., "Engineering Transition Prediction for a Hypersonic Axisymmetric Boundary Layer," *Journal of Aircraft*, Vol. 31, No. 6, Nov. 1994, pp. 1358–1364. doi:10.2514/3.46659

[34] Chen, F.-J., Malik, M. R., and Beckwith, I. E., "Boundary-Layer Transition on a Cone and Flat Plate at Mach 3.5," *AIAA Journal*, Vol. 27, No. 6, 1989, pp. 687–693. doi:10.2514/3.10166

[35] Candler, G. V., "Hypersonic Nozzle Analysis Using an Excluded Volume Equation of State," *38th AIAA Thermophysics Conference*, AIAA Paper 2005–5202, June 2005.

[36] MacLean, M., Candler, G., and Holden, M., "Numerical Evaluation of Flow Conditions in the LENS Reflected Shock-Tunnel Facilities," *43rd Aerospace Sciences Meeting & Exhibit*, AIAA Paper 2005-0903, Jan. 2005.

[37] MacLean, M., Mundy, E., Wadhams, T., Holden, M., Johnson, H., and Candler, G., "Comparisons of Transition Prediction Using PSE-Chem to Measurements for a Shock Tunnel Environment," *37th AIAA Fluid Dynamics Conference & Exhibit*, AIAA Paper 2007-4490, June 2007.

[38] Johnson, H., Alba, C., Candler, G., MacLean, M., Wadhams, T., and Holden, M., "Boundary Layer Stability Analysis to Support the HIFiRE Transition Experiment," *45th Aerospace Sciences Meeting & Exhibit*, AIAA Paper 2007-0311, Jan. 2007.

[39] MacLean, M., Wadhams, T., Holden, M., and Johnson, H., "A Computational Analysis of Ground Test Studies of the HIFiRE-1 Transition Experiment," *46th Aerospace Sciences Meeting & Exhibit*, AIAA Paper 2008-0641, Jan. 2008.

[40] Spalart, P., "Trends in Turbulence Modeling," *Fluids 2000*, AIAA Paper 2000–2306, June 2000.

[41] Dhawan, S., and Narasimha, R., "Some Properties of Boundary Layer Flow During Transition from Laminar to Turbulent Motion," *Journal of Fluid Mechanics*, Vol. 3, No. 4, 1958, pp. 418–436. doi:10.1017/S0022112058000094

[42] Wilcox, D. C., "A Model for Transitional Flows," *15th Aerospace Sciences Meeting*, AIAA Paper 77-126, Jan. 1977.

[43] Warren, E., Harris, J., and Hassan, H., "Transition Model for High-Speed Flow," *AIAA Journal*, Vol. 33, No. 8, Aug. 1995, pp. 1391–1397. doi:10.2514/3.12687

[44] Papp, J. L., Kenzakowski, D. C., and Dash, S. M., "Extensions Of A Rapid Engineering Approach to Modeling Hypersonic Laminar to Turbulent Transitional Flows," *43rd Aerospace Sciences Meeting & Exhibit*, AIAA Paper 2005-0892, Jan. 2005.

[45] Van Driest, E. R., "The Problem of Aerodynamic Heating," *Aeronautical Engineering Review*, Vol. 15, Oct. 1956, pp. 26–41.

[46] Holden, M. S., "Shock Wave–Turbulent Boundary Layer Interaction in Hypersonic Flow," *10th AIAA Aerospace Sciences Meeting*, AIAA Paper 72-74 , Jan. 1972.

[47] Goyne, C. P., Stalker, R. J., and Paull, A., "Skin-Friction Measurements in High-Enthalpy Hypersonic Boundary Layers," *Journal of Fluid Mechanics*, Vol. 485, 2003, pp. 1–32. doi:10.1017/S0022112003003975

[48] Huang, P. G., Bradshaw, P., and Coakley, T. J., "Turbulence Models for Compressible Boundary Layers," *AIAA Journal*, Vol. 32, No. 4, April 1994, pp. 735–740. doi:10.2514/3.12046

[49] Holden, M. S., "A Study of Flow Separation in Regions of Shock Wave-Boundary Layer Interaction in Hypersonic Flow," *11th AIAA Fluid and Plasma Dynamics Conference*, AIAA Paper 78-1169, July 1978.

[50] Sarkar, S., Erlebacher, G., Hussaini, M. Y., and Kreiss, H. O., "The Analysis and Modeling of Dilational Terms in Compressible Turbulence," NASA CR-181959, 1989.

[51] Wilcox, David C., *Turbulence Modeling for CFD*, 3rd ed., DCW Industries, Inc., La Canada, CA, Nov. 2006.

[52] Edwards, J. R., Choi, J. I., and Boles, J. A., "Large-Eddy/Reynolds-Averaged Navier–Stokes Simulation of a Mach 5 Compression-Corner Interaction," *AIAA Journal*, Vol. 46, No. 4, April 2008, pp. 977–991. doi:10.2514/1.32240

[53] Rung, T., Bunge, U., Schatz, M., and Thiele, F., "Restatement of the Spalart–Allmaras Eddy–Viscosity Model in Strain–Adaptive Formulation," *AIAA Journal*, Vol. 41, No. 7, July 2003, pp. 1396–1399. doi:10.2514/2.2089

[54] Barnhardt, M., and Candler, G., "Detached Eddy Simulation of Hypersonic Base Flows During Atmospheric Entry," *9th AIAA/ASME Joint Thermophysics and Heat Transfer Conference*, AIAA Paper 2006-3575, June 2006.

[55] *Guide for the Verification and Validation of Computational Fluid Dynamics Simulations*, AIAA, Reston, VA, G-077-1998, 1998.

[56] Sinha, K., Mahesh, K., and Candler, G., "Modeling the Effect of Shock Unsteadiness in Shock/Turbulent Boundary-Layer Interactions," *AIAA Journal*, Vol. 43, No. 3, March 2005, pp. 586–594. doi:10.2514/1.8611

R. Kimmel
Associate Editor